Primary radiation damage in tungsten-based high-entropy alloy: Interatomic potential and collision cascade simulations

Yangchun Chen [a], Xichuan Liao [a], Rongyang Qiu [b], Lixia Liu [c], Wangyu Hu [a], Huiqiu Deng [b],[*]

[a] *College of Materials Science and Engineering, Hunan University, Changsha 410082, China*
[b] *School of Physics and Electronics, Hunan University, Changsha 410082, China*
[c] *School of Physics, Suqian College, Suqian 223800, China*

ARTICLE INFO

ABSTRACT

Tungsten (W)-based high-entropy alloys (HEAs) have shown promising properties as nuclear fusion materials. Characterizing the primary damage is a critical step in describing and revealing the irradiation-induced damage and radiation resistance mechanism. However, there are a limited number of studies on collision cascades and primary radiation damage in W-based HEAs, owing to the large amount of calculations involved and a lack of appropriate interatomic interaction potentials. In this work, we developed a semi-empirical interatomic potential for W–Ta–Cr–V. By using the developed potential, molecular dynamics simulations of collision cascades in W-based HEAs were performed to assess the primary damage due to irradiation. Based on experimental samples, we reported defect production in $W_{38}Ta_{36}Cr_{15}V_{11}$ and compared it to pure W for primary knock-on atom with energies ranging from 1 keV to 100 keV. Our findings showed that the number of FPs at the thermal spike and the number of surviving FPs at the end of the cascade in $W_{38}Ta_{36}Cr_{15}V_{11}$ are more than those in pure W, mainly due to the lower threshold displacement energy, melting temperature, and formation energy of point defects. Collision cascades in the $W_{38}Ta_{36}Cr_{15}V_{11}$ are less likely to result in the formation of dislocation loops compared to pure W. After collision cascade, in $W_{38}Ta_{36}Cr_{15}V_{11}$, the concentrations of Cr and V atoms in defects is significantly higher than their corresponding concentrations in the system, showing an aggregation tendency. The current collision cascade results provide insights into the primary damage of W-based HEA system under irradiation and should provide reliable guidance for describing the primary damage source terms needed in the kinetic models used to simulate radiation-induced microstructural evolution.

1. Introduction

In recent years, environmental and energy-related problems have become more serious for natural environments. A promising solution to this problem is the development of controllable deuterium tritium nuclear fusion energy. Its ultimate safe application depends partially on the development of key materials for fusion devices. Refractory metal tungsten (W) is the leading candidate for use in plasma-facing components of future fusion reactors, such as ITER (International Thermonuclear Experimental Reactor), DEMO (Demonstration Power Station) and CFETR (China Fusion Engineering Test Reactor) [1–3]. It offers many advantages, such as high melting point, high thermal conductivity, good chemical stability, low deuterium/tritium retention rate, and high sputtering resistance to energetic particles.

Nevertheless, pure W material also has several shortcomings that

need to be addressed. Some of its major shortcomings include high ductile-to-brittle transition temperature, low machinability and manufacturability, low temperature brittleness, pronounced embrittlement when irradiated with high-energy neutrons, and formation of bubbles, blisters, and fuzzy nanostructures with high-fluxes helium and deuterium ion irradiation [4–6]. Consequently, several strategies, such as adding different alloying elements to W (e.g., W–Re, W–Ta, W–V, and W–Ti binary alloys), W-based composites, or nanostructure-engineered W, for improving the performance of W have been proposed and investigated [7–10]. However, experimental studies in various aspects of binary alloys have revealed numerous constraints. The ductile-to-brittle transition temperature of most alloys is higher compared to pure W; only Re is known to improve the ductility of W by solid solution; and irradiation-induced embrittlement in W–Re and W–Os alloys due to the formation of σ- and χ-phase precipitates [2,11].

Similarly, nanocrystalline W samples exhibit significant helium bubble formation at grain boundaries, resulting in poorer mechanical properties at operational temperatures, limiting their applicability in fusion environments [10,12]. Laminated, fiber- and net-reinforced W-based composites can improve toughness and ductility, but they have an anisotropic configuration and low relative densities [13–15].

In contrast to traditional approaches, the development of multi-component concentrated solid solution alloys, including medium-entropy and high-entropy alloys (HEAs), has provided new ideas for the design of advanced W materials for fusion reactors [16–21]. Senkov et al. [22] designed and prepared two typical alloys, W$_{25}$Ta$_{25}$Nb$_{25}$Mo$_{25}$ and W20Ta20Nb20Mo20V20, to create W-containing refractory HEAs. The yield strength of these two alloys at room-temperature was measured to be 1058 MPa and 1246 MPa, respectively. These alloys also possess an excellent high-temperature yield strength of 405 MPa and 477 MPa, respectively, measured at 1600 °C; these values are better than that of nickel-based superalloys [22]. Waseem et al. [20,21,23–26] developed W-based quinary refractory HEAs of W$_x$TaTiVCr (x = 30 to 90). Among these W-based alloys, W50(TaTiVCr)50 is of particular interest for fusion applications due to its composition of low activation elements, nearly full relative density, homogeneous microstructure, and ~2000 MPa room temperature compressive strength, ~800 HV hardness and ~7.7 MPa m$^{1/2}$ fracture toughness [21,26]. In addition, W50(TaTiVCr)50 showed only minor damage in the form of randomly dispersed black dots and precursors of helium bubbles and dislocations after helium ion irradiation (with 200 keV helium ions irradiated to a maximum fluence of 10^{21} ions/m^2). The hardness of the alloy increased by 3.3 GPa, i.e., from 11.6 GPa to 14.9 GPa, due to the microstructural changes caused by irradiation [21]. Under the given experimental conditions, the relatively better irradiation resistance of W50(TaTiVCr)50 compared to W suggests its potential applications in fusion plasma.

Recently, El-Atwani et al. [16,27] developed W38Ta36Cr15V11, a body-centered cubic low-activation refractory W-based HEA. The in-situ and ex-situ irradiation analysis of W38Ta36Cr15V11 (by 1 MeV Kr^{+2} ions up to 1.6 dpa and 8 dpa at room temperature and 1073 K, and 3 MeV Cu ions up to 17 dpa at 773 K and 1050 K, respectively) demonstrated high radiation tolerance [16]. The authors did not find any evidence of radiation-induced dislocation loops in the microstructure. According to nanomechanical testing, the as-deposited samples have a high hardness of 14 GPa with near negligible irradiation hardening. The authors also tested the W–Ta–Cr–V alloy under low-energy helium implantation up to a fluence of 1.25×10^{17} $\frac{-2}{cm}$ at 1223 K [27]. They observed a uniform distribution of small bubbles, and bubble damage reached a plateau at high fluences. No preferential bubble formation was observed on the grain boundaries. With respect to the overall damage (both grain matrices and grain boundaries), the response of W–Ta–Cr–V HEA to helium implantation is remarkably better than that pure nanocrystalline W and other studied alloys [27]. However, this quaternary W–Ta–Cr–V HEA has shown the formation of Cr- and V-rich precipitates when irradiated up to 8 dpa with 1 MeV Kr ions [16]. Such a precipitation is not desired for future nuclear materials, which could be detrimental to mechanical properties in terms of embrittlement, therefore alloys with higher phase stability composes a major criterion for design and selection of fusion materials. Through experiments, El-Atwani et al. found that adding Hf into the W–Ta–Cr–V alloy, forming the W–Ta–Cr–V–Hf quinary HEA, can significantly improve the thermodynamic stability of the quaternary alloy under irradiation [28].

These findings show that W-based HEAs have good resistance to ion irradiation, as evidenced by the inhibition of dislocation loop formation, formation of smaller and more uniformly distributed helium bubbles, no preferential helium bubble segregation at grain boundaries, and the presence of low activation elements, indicating that these alloys have a high potential for becoming new irradiation-resistant candidate materials for fusion reactors. Therefore, there is an urgent need to conduct research on neutron irradiation resistance and irradiation resistance mechanism of W-based HEAs. Due to the scarcity of fusion neutron

sources and the difficulty of conducting experiments on numerous alloy compositions that may be used in W-based HEAs, computational simulations are required to guide experiments and understand the atom-level mechanisms that give HEAs their unique properties. However, most modeling techniques are challenging due to their chemical complexity. In this regard, density functional theory (DFT) is an invaluable tool for quantifying fundamental material and defect properties, but it is computationally too demanding for large-scale atomistic simulations. Large-scale atomic simulations, such as using the molecular dynamics (MD) and Monte Carlo (MC) methods, have proved to be an effective tool for understanding material properties under neutron irradiation as well as explaining or extending experimental observations [29]. Nevertheless, these simulations rely on interatomic potentials to describe the interactions between atoms. Developing interaction potentials for an HEA with many elements is extremely difficult because of the numerous cross-species interactions.

Recently, Li et al. [30] developed a spectral neighbor analysis machine-learning potential for the W−Ta–Nb−Mo system. They used it to study the fundamental properties of screw and edge dislocations and found that Nb segregates to grain boundaries. Byggmästar et al. [31] developed a Gaussian approximation machine-learning interatomic potential for the W–Ta–Nb–Mo–V quinary system to study the segregation and defect structure in the equiatomic W–Ta–Nb–Mo–V HEA. Collision cascades generate a large number of initial defects in materials when exposed to high-energy neutrons, such as isolated or clustered vacancies and interstitials, large dislocation loops, and vacancy clusters or voids. The generation, distribution, number, and structure of defects in the collision cascade stage are critical for determining the mechanisms of irradiation resistance. However, there are a limited number of studies on collision cascades and primary radiation damage in W-based HEAs, owing to the large amount of calculations involved (for example, the system contains millions of atoms in high-energy collision cascade, and the number of statistics under each condition must be reached dozens of times) and a lack of appropriate interatomic interaction potentials.

In this paper, we developed a semi-empirical interatomic potential for W–Ta–Cr–V; this is a significant step toward an atomic-scale investigation of W-based HEAs. In addition, we carried out a series of collision cascade simulations for W38Ta36Cr15V11 HEA in the primary knock-on atoms (PKA) energy range of 1–100 keV using the developed potential and the MD method. We report the production of defects, including point defects, defect clusters, and dislocation loops, created by collision cascade in W38Ta36Cr15V11 and compared the results to those of pure W. We believe our findings will provide a basis for understanding the primary damage of W-based HEA system under irradiation and for simulating the long-term evolution of defects in the subsequent annealing process.

2. Methodology

2.1. Interatomic potential

This work aimed to fit an interatomic potential that describes the quaternary W–Ta–Cr–V system. The atomic interactions are expressed using the Finnis–Sinclair (FS) formalism [32,33], which is widely used to describe metals and their alloys. The total potential energy U of a system containing N atoms is given by

$$U = \frac{1}{2} \sum_{\substack{i,j=1 \\ j \neq i}}^{N} V_{t_i t_j}(r_{ij}) + \sum_{i=1}^{N} F_{t_i}(\rho_i). \tag{1}$$

Here, the first term is the sum of pair potential $V_{t_i t_j}(r_{ij})$ as a function of the distance r_{ij} between atoms i and j with atomic types t_i and t_j. The second term is the sum of embedding energies $F_{t_i}(\rho_i)$ as a function of the host density ρ_i, which is expressed as the sum of contribution $f_{t_i t_j}(r_{ij})$ from

all neighbouring atoms j:

$$\rho_i = \sum_{j=1, j \neq i}^{N} f_{t_i t_j}(r_{ij}). \tag{2}$$

A complete FS description of the quaternary W–Ta–Cr–V system requires 24 functions. The F_W, F_{Ta}, F_{Cr}, and F_V denote the embedding energy functions of W, Ta, Cr, and V respectively. The V_{WW}, V_{TaTa}, V_{CrCr} and V_{VV} denote the pair potential functions, and the f_{WW}, f_{TaTa}, f_{CrCr} and f_{VV} denote the electron density functions of W, Ta, Cr, and V respectively. The V_{WTa}, V_{WCr}, V_{WV}, V_{TaCr}, V_{TaV} and V_{CrV} denote the cross-interaction pair potential functions, and the f_{WTa}, f_{WCr}, f_{WV}, f_{TaCr}, f_{TaV} and f_{CrV} denote the cross-interaction electron density functions for alloys. Our group has developed the W [34,35], Ta [36], and V [37] unary and the W–Ta [36], W–V [37], and Ta–V [38] binary potentials based on the FS potential formalism. These potential functions were used to develop the W–Ta–Cr–V potential, and the rest of the functions (F_{Cr}, V_{CrCr}, V_{WCr}, V_{TaCr}, V_{CrV}, f_{CrCr}, f_{WCr}, f_{TaCr}, f_{CrV}) were fitted in this work.

The embedding energy function is calculated using

$$F(\rho) = -\sqrt{\rho}. \tag{3}$$

The pair potential function $V_{AA}(r)$ and electron density function $f_{AA}(r)$ for pure elements are defined as follows:

$$V_{AA}(r) = \sum_{k=1}^{n_k} a_k (r_k - r)^3 H(r_k - r), \tag{4}$$

$$f_{AA}(r) = \sum_{k=1}^{N_k} A_k (R_k - r)^3 H(R_k - r), \tag{5}$$

where, $H(x)$ represents the Heaviside step function, a_k and A_k denote the knots coefficients, and r_k and R_k denote the positions of cubic spline knots, respectively.

Before fitting the cross-interaction potential functions, the following invariant transformations [39,40] were applied for pure element potentials:

$$\begin{cases} f_{AA}^{eff}(r) = S \times f_{AA}(r) \\ F^{eff}(\rho) = F\left(\dfrac{\rho}{S}\right) + \dfrac{C}{S}\rho \\ V_{AA}^{eff}(r) = V_{AA}(r) - 2C \times f_{AA}(r) \end{cases} . \tag{6}$$

Here, S denotes a constant determined by an equilibrium density $\rho_0 = 1$, and the constant D is determined by $F^{eff\prime}(\rho_0) = 0$. Based on the transformation, the pair potential is the effective two-body potential, and the electron density value at the corresponding site is comparable for different elements in an alloy case. The transformation described above has no effect on the properties of pure element potentials and provides a useful approach to fitting alloy potentials.

The cross-interaction pair potential function $V_{AB}(r)$ is defined by the linear combination of the pair potential functions of pure elements:

$$V_{AB}(r) = \frac{1}{2}\left[u_a V_{AA}^{eff}\left(r\frac{r_a}{r_c}\right) + u_b V_{BB}^{eff}\left(r\frac{r_b}{r_c}\right)\right], \tag{7}$$

$$r_c = \frac{1}{2}[r_1(A) + r_1(B)]. \tag{8}$$

Where, u_a, u_b, r_a and r_b denote fitting parameters, and $r_1(A)$ and $r_1(B)$ represent the first-neighbour distance of element A and element B. This cross-interaction pair potential function has been widely used in our previous work [34,37,41,42]. The cross-interaction electron density function is taken as

$$f_{AB}(r) = \sum_{k=1}^{N_k} Q_k (R_k - r)^3 H_s (R_k - r). \tag{9}$$

All the pair potential functions are joined with the Ziegler–Biersack–Littmark (ZBL) universal function [43] through a connection function to appropriately simulate collision cascades, especially for accurate description of the interaction induced by two atoms at a short-range distance. The new pair potential can be described as

$$V(r) = \begin{cases} V_{ZBL}, & r \leq r_m \\ V_{Connect}, & r_m < r < r_n \\ V_{Original}, & r \geq r_n \end{cases} . \tag{10}$$

The ZBL potential [43] is given by:

$$V_{ZBL}(r_{ij}) = \frac{1}{4\pi\varepsilon_0} \frac{Z_i Z_j e^2}{r_{ij}} \varphi(r_{ij} / a), \tag{11}$$

$$\begin{aligned} \varphi(x) = \ & 0.18175 e^{-3.19980x} + 0.50986 e^{-0.94229x} + 0.28022 e^{-0.4029x} \\ & + 0.02817 e^{-0.20162x}, \end{aligned} \tag{12}$$

$$a = \frac{0.4685335}{Z_i^{0.23} + Z_j^{0.23}}. \tag{13}$$

The connect function has the form:

$$V_{Connect}(r) = e^{\left(C_0 + C_1 r + C_2 r^2 + C_3 r^3\right)}, \tag{14}$$

where the C_i coefficients are determined by the continuity of the pair potential function and its first derivative.

The simulated annealing method [44] was used in the fitting process. The potential parameters were determined by minimizing the weighted mean-squared deviation of the selected properties from their target values. Lattice constant, bulk modulus, elastic constants, cohesive energy, vacancy formation energy, interstitial formation energy, and the equation of state for body-centered cubic lattice (Rose's equation [45]) were among the fitted target properties for pure elements. The formation energies and binding energies of some typical irradiation defects in reference matrices, including the formation energy of a single solute substitutional atom, the binding energy of a solute substitution atom with a vacancy, and the binding energy of a solute substitution atom with a self-interstitial atom, were considered for cross-interactions. A detailed definition of these typical defect energies can be found in our previous paper [34]. The formation energies or binding energies of various defects were obtained using the dynamics fitting approach. The simulation box used in the fitting process is of $10a_0 \times 10a_0 \times 10a_0$ (a_0 denotes the equilibrium lattice constant). Defect configurations were created by adding or removing atoms as needed. Table 1 shows the optimized potential parameters, as well as the parameters for the ZBL connection function. Fig. 1 depicts the curves of all potential functions, demonstrating the smoothness of the potential functions across all regions.

2.2. Cascade simulation

Collision cascade simulations were performed in $W_{38}Ta_{36}Cr_{15}V_{11}$, which was selected based on experimental studies of W-based HEA samples [16]. Our MD simulations were performed using the Large-scale Atomic/Molecular Massively Parallel Simulator (LAMMPS) code [46]. The single cascade were simulated using PKA energies from 1 keV to 100 keV. A sample was equilibrated for 20 ps at 300 K and zero pressure with the NPT (constant number of atoms, pressure and temperature) ensemble before initiating the cascade. This initial atom block was then used as a starting point for cascade simulations as well as a reference for the defect analysis. The cascade was started by imparting a kinetic energy to a randomly selected PKA along a high-index direction $\langle 135 \rangle$ in order to avoid channeling. The microcanonical ensemble (NVE) was used to follow a cascade evolution with a variable time step. No electronic stopping or electron-phonon coupling was included in the simulations. To obtain statistically meaningful results, 25–50 MD runs were carried out at each PKA energy. A total of 600 cascading events occurred: 300 cascading events occurred in $W_{38}Ta_{36}Cr_{15}V_{11}$ and 300

Table. 1

The potential parameters for Cr–Cr, W–Cr, Ta–Cr, and V–Cr interactions are listed. Potential parameters for W–W, Ta–Ta, V–V, W–Ta, W–V, and Ta–V interactions remain unchanged and are available in our previous papers [35–38]. The table also includes the parameters of the connection function, which connects the original equilibrium part with the ZBL potential. The units of distance and energy are Å and eV, respectively.

	Cr–Cr		
A_1 (R_1)	+0.0615258950036 (4.85)	a_1 (r_1)	+0.0518644422838 (4.85)
A_2 (R_2)	−0.1228069662212 (4.55)	a_2 (r_2)	−0.0190106319153 (4.55)
A_3 (R_3)	+0.0617479427545 (4.25)	a_3 (r_3)	+0.0012628894303 (4.25)
A_4 (R_4)	+0.0442023494989 (3.95)	a_4 (r_4)	−0.5072215201487 (3.95)
A_5 (R_5)	+1.2496100449297 (3.65)	a_5 (r_5)	−0.0998008380255 (3.65)
A_6 (R_6)	−2.6314325647721 (3.35)	a_6 (r_6)	+1.0612866437035 (3.35)
A_7 (R_7)	+1.3657599101116 (3.05)	a_7 (r_7)	+2.7124660836659 (3.05)
A_8 (R_8)	−0.0161584645032 (2.75)	a_8 (r_8)	−5.3908367692149 (2.75)
A_9 (R_9)	+20.505289612359 (2.45)	a_9 (r_9)	+16.013354609702 (2.45)
A_{10} (R_{10})	−12.608427589384 (2.25)	a_{10} (r_{10})	−12.343496962697 (2.25)
S	+0.1181772097331	C	+0.1718845613581
C_0	+7.7648274782493	C_1	−2.9423503277036
C_2	0.32934078218844	C_3	−0.4941041879579
r_m	+1.0000000000000	r_n	+2.0000000000000
	W–Cr	Ta–Cr	V–Cr
A_1 (R_1)	+0.0039793869486 (4.8)	+0.0026165984088 (4.8)	+0.0014858410343 (4.8)
A_2 (R_2)	−0.0062598960477 (4.0)	+0.0176259710107 (4.0)	−0.0020704767555 (4.0)
A_3 (R_3)	+0.5723421439945 (3.2)	+0.2437132368087 (3.2)	+0.3069795893064 (3.2)
A_4 (R_4)	+0.9445286551052 (2.5)	−0.3818728502947 (2.5)	+0.9205898413300 (2.5)
u_a	+2.1130094953347	+1.1841093677922	+1.5881198194518
u_b	+3.9958253800869	+1.2785044730879	+0.5713647455436
r_a	+2.8016516265764	+2.6777130121227	+2.6366442337450
r_b	+3.6229803512290	+2.7425129285663	+2.6545407681320
r_c	+2.6176000000000	+2.6777000000000	+2.5591000000000
C_0	+8.1679608062642	+9.9467205739029	+8.9756812814390
C_1	−2.4633646693456	−4.5989881886440	−4.2945474126950
C_2	+0.4479115288467	−0.0495173535366	+0.1867402336920
C_3	−0.7949392366894	+0.0514447749652	−0.2383144731503
r_m	+1.0000000000000	+1.0000000000000	+1.0000000000000
r_n	+2.0000000000000	+2.0000000000000	+2.0000000000000

occurred in pure W for comparison. The largest simulation box contained 16 million atoms and was used to simulate the collision cascade in $W_{38}Ta_{36}Cr_{15}V_{11}$ at PKA energy of 100 keV. Table 2 summarizes cubic box size, number of atoms in the box, simulated time, and number of cascades versus PKA energy. We used the open-source application OVITO [47] for defect analysis and visualization. The Wigner–Seitz cell method [48] as implemented in OVITO was used to identify the formed interstitials and vacancies. Point defects within a fixed truncation radius were included in the same defect clusters. Based on previous studies [49, 50], halfway between the second and third nearest neighbors was selected as the cut-off distance for vacancy cluster analysis, and halfway between the third and fourth nearest neighbors was selected as the cut-off distance for the interstitial cluster analysis. The dislocation extraction algorithm (DXA) [51] was used to identify the formed dislocation loops.

3. Results and discussion

3.1. Characteristics of the W–Ta–Cr–V potential

Here, we briefly demonstrate the accuracy of the W–Ta–Cr–V potential before using it to study the primary radiation damage of $W_{38}Ta_{36}Cr_{15}V_{11}$ HEA. The lattice constants, cohesive energies, bulk moduli, and elastic constants of four BCC metals (W, Ta, Cr, and V) are shown in Table 3. As shown in the table, the calculated values of the potential are in good agreement with the experimental values [52–55]. Then, the properties of vacancy and interstitial defects in the four metals were calculated. Table 4 lists the formation energies of self-interstitial atoms. There are six possible interstitial configurations: ⟨111⟩ dumbbell, ⟨111⟩ crowdion, ⟨110⟩ dumbbell, ⟨100⟩ dumbbell, tetrahedral interstitial, and octahedral interstitial. Fig. 2 depicts the vacancy formation and migration energies of W, Ta, Cr, and V. From the results, we can see that the point defects properties calculated by the potential agree well with the DFT results [56,57].

We also predicted the formation energies of 1/2⟨111⟩ and ⟨100⟩ interstitial dislocation loops with different sizes in the four metals. The largest constructed dislocation loop contains ~300 interstitial atoms, and the smallest 1/2⟨111⟩ or ⟨100⟩ dislocation loops have 7 or 5 interstitial atoms, respectively. The calculation results are shown in Fig. 3. The 1/2⟨111⟩ loops in W, Ta, Cr, and V are energetically favored for all considered sizes, implying that the most stable configuration for an interstitial loop is a 1/2⟨111⟩ loop at low temperatures. This finding is consistent with experimental observations and DFT results [58–60].

The potential was used to determine the key properties of Ta, Cr, and V solute atoms in the BCC W matrix, and the results were compared to DFT values. Table 5 shows that the formation energies of substitutional solute atoms Ta, Cr, and V in the W matrix were −0.47 eV, 0.37 eV, and −0.37 eV, respectively. These findings agree well with the DFT calculation results [61–66]. Table 6 shows the binding energies of two substitutional solute atoms (Ta–Ta, Cr–Cr, and V–V) at the first nearest neighbor (1NN) and second neighbor (2NN) sites in the W matrix. The potential can correctly describe the repulsive or attractive interaction between two substitutional solute atoms. Table 7 shows the binding energy of a solute atom to a vacancy, the binding energy of a solute atom to a self-interstitial atom, and the binding energy of a pure solute dumbbell in the W matrix. The calculations of our potential are close to the results of DFT [63–68].

The potential was also used to predict the formation enthalpies of BCC binary disordered solid solutions in the W–Ta–Cr–V system. Fig. 4 depicts the calculation results. The figure also depicts the enthalpies of the formation of binary alloys derived from DFT and Cluster Expansion (CE) simulations [16,69]. The potential calculated formation enthalpies of W–Ta, W–V, and V–Cr systems were negative, while those of W–Cr, Ta–Cr, and V–Cr systems were positive. Enthalpy values close to zero indicate the possibility of solid solution formation, while negative values indicate a tendency to form intermetallic phases and positive values indicate a tendency to atoms segregation. The present potential calculation results agree with those obtained using the DFT and CE methods.
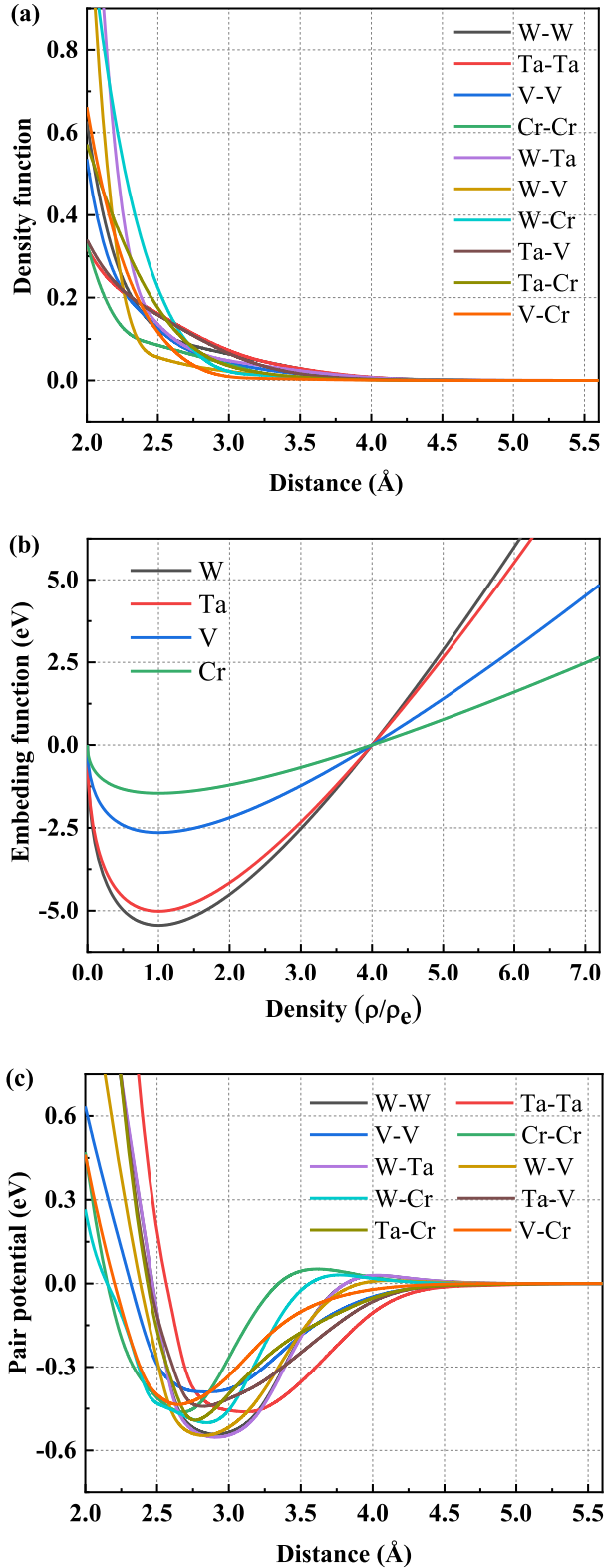
Fig. 1. Dependence of the potential functions on atomic distance or electronic density: (a) density functions, (b) embedding functions and (c) pair potentials.

Table. 2
Lists the PKA energy, simulation time, cubic box size, number of atoms in the box, and number of cascades.

	PKA energy (keV)	Simulation time (ps)	Box side length (*a*)	Number of atoms (10³)	Cascade events
$W_{38}Ta_{36}Cr_{15}V_{11}$	1	40	60	432	25
	5	40	60	432	25
	10	40	80	1024	25
	15	40	80	1024	25
	25	50	100	2000	50
	50	60	120	3456	50
	75	80	140	5488	50
	100	100	200	16,000	50
W	1	40	40	128	25
	5	40	40	128	25
	10	40	60	432	25
	15	40	60	432	25
	25	50	80	1024	50
	50	60	100	2000	50
	75	80	110	2662	50
	100	100	120	3456	50

Table. 3
Lattice constant, cohesive energy, bulk modulus and elastic constant of the four BCC component metals. Values in the first line (plain font) are calculated using the potential, and values in the second line (italicized value) are the experimental data form Refs. [52–55].

	W	Ta	Cr	V
a (Å)	3.1652	3.3039	2.88	3.03
	3.1652	*3.3039*	*2.88*	*3.03*
E_c (eV)	8.9	8.1	4.1	5.31
	8.9	*8.1*	*4.1*	*5.31*
B (GPa)	310	194	198	155
	310	*194*	*190*	*157*
C_{11} (GPa)	522	267	382	234
	522	*266*	*391*	*232*
C_{12} (GPa)	204	158	107	115
	204	*158*	*90*	*119*
C_{44} (GPa)	161	87	92	45
	161	*87*	*103*	*46*

Table. 4
Self-interstitial atom formation energies of the four BCC component metals. Values in the first line (plain font) are calculated using the potential, and values in the second line (italicized value) are the DFT data form Ref. [56].

	W	Ta	Cr	V
E^f<111>dumbbell	9.58	5.75	5.69	3.38
	9.55	*5.83*	*5.69*	*3.37*
E^f<111>crowdion	9.60	5.77	5.68	3.37
	9.55	*5.84*	*5.66*	*3.37*
E^f<110>dumbbell	9.84	6.15	5.43	3.57
	9.84	*6.38*	*5.67*	*3.65*
E^f<100>dumbbell	11.20	6.32	7.04	3.75
	11.49	*7.00*	*6.64*	*3.92*
E^foctahedral	10.81	6.24	6.94	3.66
	11.68	*7.09*	*6.72*	*3.96*
E^ftetrahedral	10.45	6.23	6.56	3.69
	11.05	*6.77*	*6.19*	*3.84*

The formation energy of interstitials in the $W_{38}Ta_{36}Cr_{15}V_{11}$ HEA calculated by our potential is shown in Fig. 5. We relaxed 400 HEA systems, and each system had one interstitial atom inserted at random. Relaxation mainly produces dumbbell configurations of atom pairs. Fig. 5(a) and (b) show the distributions of relaxed dumbbell configurations and formation energies, respectively. Our findings showed that W–W, W–Ta, and Ta–Ta exhibited the highest formation energies, while Cr–Cr, Cr–V, and V–V exhibited the lowest formation energies among all interstitial types. There is a clear preference for Cr- and V-containing interstitial dumbbells, specifically Cr–Cr, Cr–V, and V–V dumbbells, which account for the vast majority of stable interstitials. In the experiment, the irradiated $W_{38}Ta_{36}Cr_{15}V_{11}$ alloy revealed precipitates enriched in Cr and V [16]. In Zhao et al.'s study,
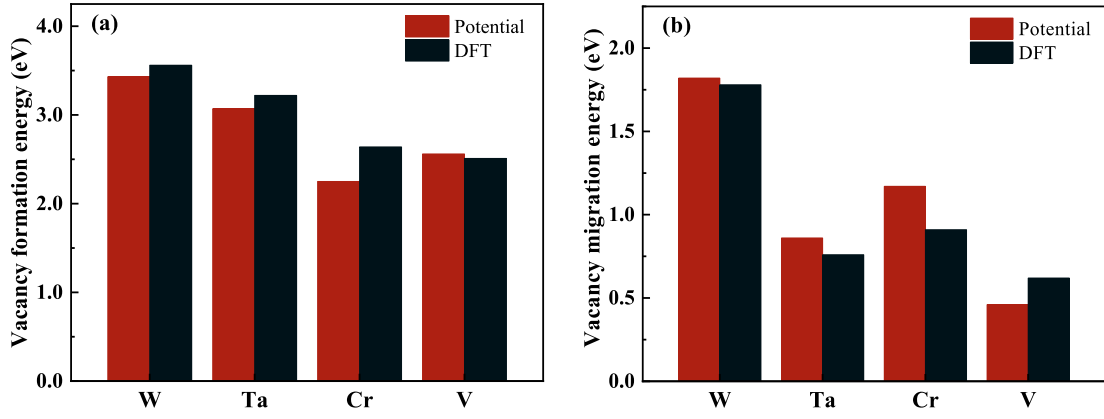
Fig. 2. (a) Vacancy formation energies and (b) vacancy migration energies of the four BCC component metals. The DFT data are obtained from Refs. [56,57].
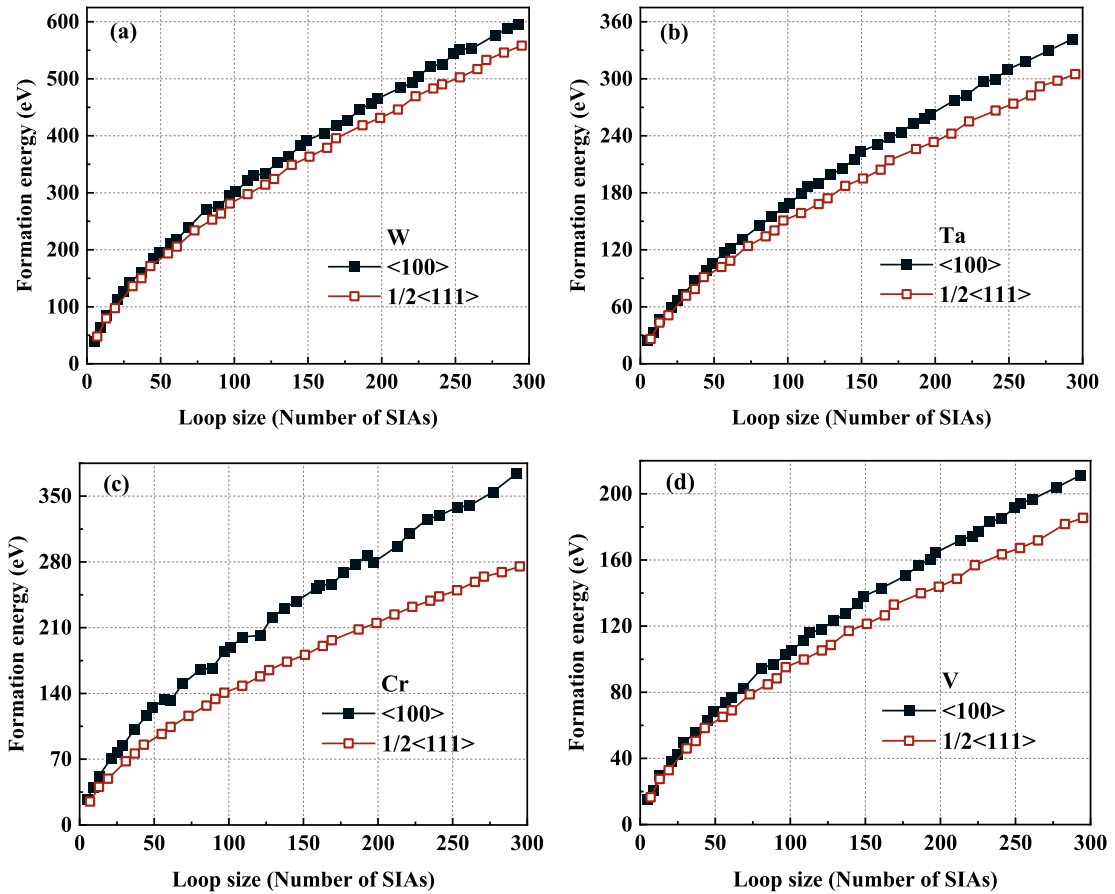

Fig. 3. Formation energies of $1/2<111>$ and $\langle100\rangle$ interstitial dislocation loops in W, Ta, Cr and V calculated by the present potential.

Table. 5
Formation energies of substitutional solute atoms Ta, Cr and V in the bcc W matrix.

Property	Potential	DFT[61–66]
E^f_{Ta} (eV)	−0.47	−0.45, −0.47
E^f_{Cr} (eV)	0.37	0.36
E^f_{V} (eV)	−0.37	−0.43, −0.45

Table. 6
Binding energies of two substitutional solute atoms at the first nearest-neighbor (1NN) and second neighbor (2NN) sites in the bcc W matrix.

Property	Potential	DFT[62,65]
$E^b_{\text{Ta–Ta\_1nn}}$ (eV)	−0.13	−0.09
$E^b_{\text{Ta–Ta\_2nn}}$ (eV)	−0.02	−0.04
$E^b_{\text{Cr–Cr\_1nn}}$ (eV)	−0.06	−0.07
$E^b_{\text{Cr–Cr\_2nn}}$ (eV)	−0.02	−0.04
$E^b_{\text{V–V\_1nn}}$ (eV)	0.06	0.01
$E^b_{\text{V–V\_2nn}}$ (eV)	0.04	0.04

the DFT results showed that the formation energies of Cr- and V-containing interstitials in equiatomic WTaCrV alloy are also the lowest [70]. The prediction of our potential is consistent with the experimental

Table. 7

Binding energies of solute atoms with vacancy and interstitial atoms in the bcc W matrix.

Property	Potential	DFT[63–68]
E^b_{Ta-Vac} (eV)	−0.06	−0.04
E^b_{Cr-Vac} (eV)	0.01	−0.02
E^b_{V-Vac} (eV)	−0.13	−0.20
$E^b_{Ta-W \langle 111 \rangle}$ (eV)	−0.59	−0.64
$E^b_{Cr-W \langle 110 \rangle}$ (eV)	2.06	2.98
$E^b_{V-W \langle 110 \rangle}$ (eV)	1.49	1.79
$E^b_{Ta-Ta \langle 110 \rangle}$ (eV)	−0.59	N/A
$E^b_{Cr-Cr \langle 110 \rangle}$ (eV)	2.71	3.06
$E^b_{V-V \langle 110 \rangle}$ (eV)	2.48	2.32

phenomena and DFT results.

3.2. Collision cascades in $W_{38}Ta_{36}Cr_{15}V_{11}$

A series of atomic collision cascade simulations were run over a PKA energy range of 1 keV to 100 keV. The defect production in $W_{38}Ta_{36}Cr_{15}V_{11}$, including Frenkel pairs (FPs), vacancy and interstitial clusters, and dislocation loops, was reported and compared to pure W.

Fig. 6 shows the time evolution of the average and standard deviation of FPs produced by the collision cascade at PKA energies of 1 keV, 5 keV, 10 keV, 15 keV, 25 keV, 50 keV, 75 keV, and 100 keV. As shown in the figure, the number of FPs rapidly increases at first and reaches a maximum at the end of the ballistically-induced displacement phase of a cascade, forming a so-called thermal spike. Then, the number of FPs
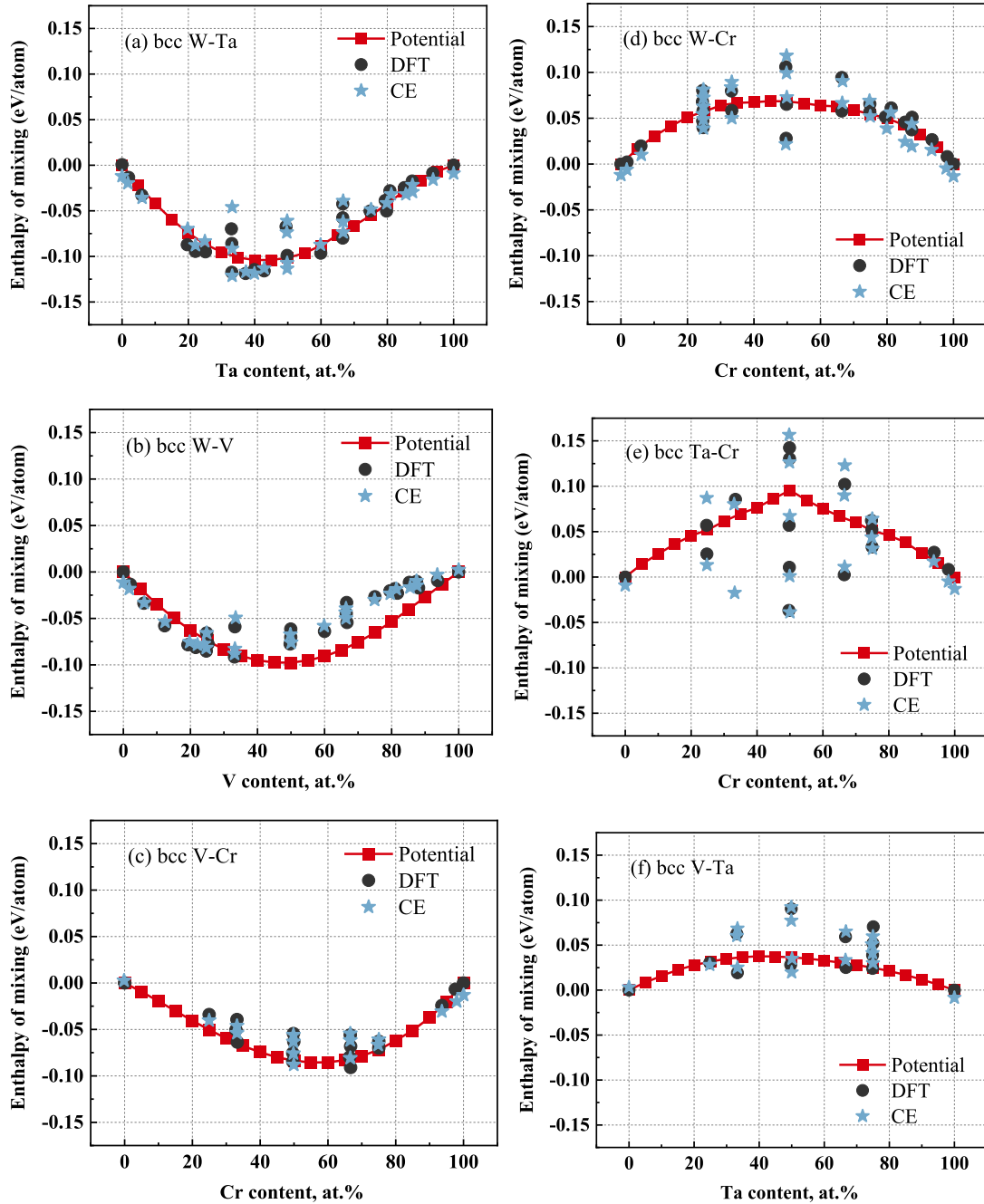

Fig. 4. Formation enthalpies of binary solid solutions in the W–Ta–Cr–V system calculated by the present potential. The enthalpies of formation of binary alloys obtained from DFT and cluster expansion (CE) simulations [16,69] are also shown in the figure.
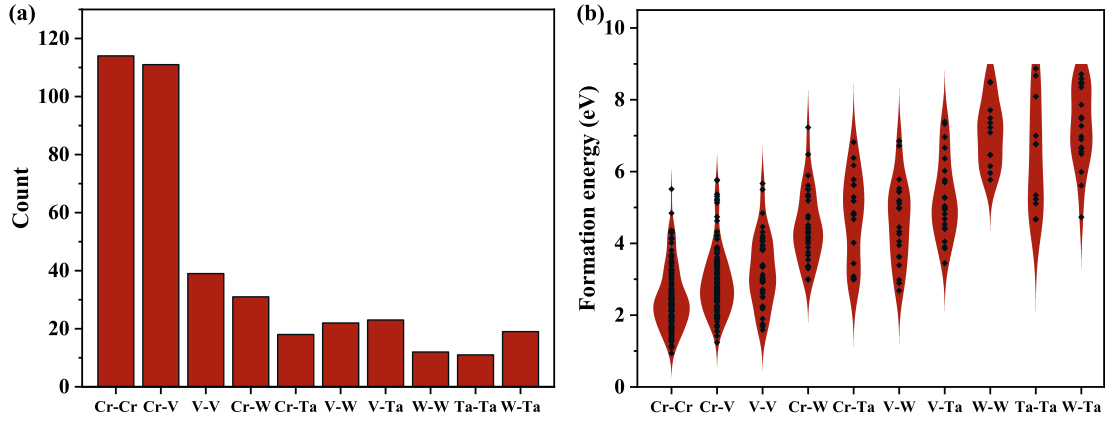
Fig. 5. Distribution of stable self-interstitial dumbbell atoms in $W_{38}Ta_{36}C_{15}V_{11}$. (a) Elements making up the stable interstitial dumbbells, and (b) formation energies distribution of interstitial dumbbells. The number of calculations is 400.
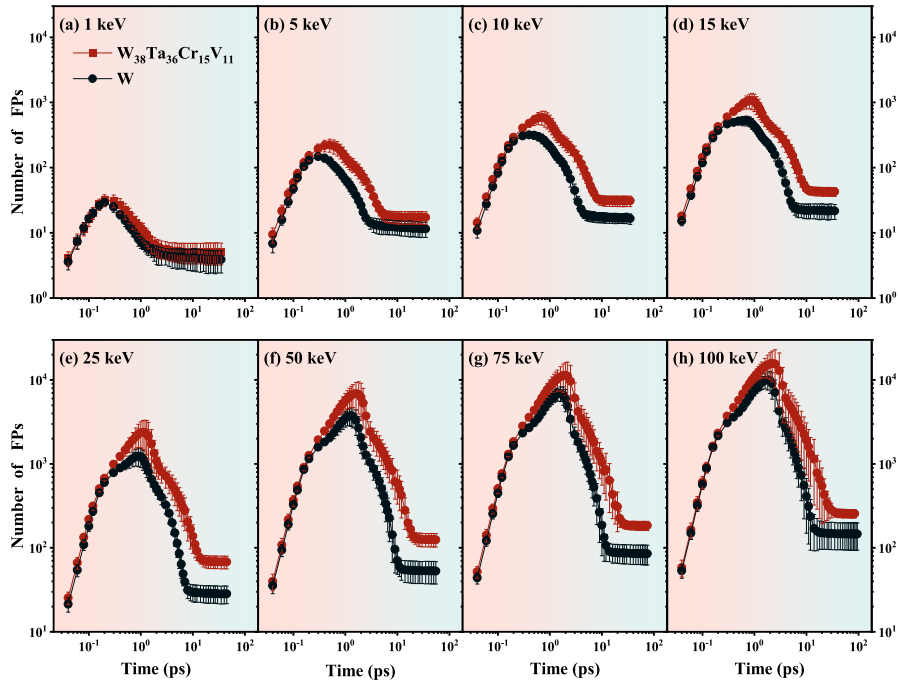

Fig. 6. The evolutions of average numbers of FPs in $W_{38}Ta_{36}Cr_{15}V_{11}$ and W as a function of time for PKA energies of (a) 1 keV, (b) 5 keV, (c) 10 keV, (d) 15 keV, (e) 25 keV, (f) 50 keV, (g) 75 keV, and (h) 100 keV.

begins to decline. Within the simulation time, the number of FPs generated in $W_{38}Ta_{36}Cr_{15}V_{11}$ and pure W at each PKA energy has reached a steady state.

Fig. 7 shows the number of FPs at the thermal spike and the number of surviving FPs at the end of the cascade as a function of PKA energy. The data points denote the mean values and the error bars represent the standard deviations after averaging over all cascades for each case. First, we verified our simulation results for pure W by comparing them with the results of Setyawan et al. [71] that were obtained via the potential of Juslin [72]. This W potential is derived from the Ackland potential [33]. Fig. 7(b) shows that the results are in good agreement with the results of Setyawan et al. regarding the surviving FPs in pure W. As shown in Fig. 7, the number of FPs at the thermal spike and the number of surviving FPs at the end of the cascade in $W_{38}Ta_{36}Cr_{15}V_{11}$ are more than those in pure W. For example, the average numbers of FPs at the thermal spike in $W_{38}Ta_{36}Cr_{15}V_{11}$ under PKA energy of 5 keV, 25 keV, 50 keV, and 100 keV are about 230, 2502, 7341, and 17,872, respectively. These

values are significantly higher than the corresponding values of 150, 1266, 3819, and 10,464 in pure W. The average numbers of surviving FPs at the end of the cascade in $W_{38}Ta_{36}Cr_{15}V_{11}$ under PKA energy of 5 keV, 25 keV, 50 keV, and 100 keV are about 17, 68, 125, and 255 respectively; these values are also higher than the corresponding values of 12, 29, 54, and 147 in pure W.

$W_{38}Ta_{36}Cr_{15}V_{11}$ exhibited more number of FPs at the thermal spike than that in pure W. This can be related to the differences in threshold displacement energies and melting temperatures between the two materials. Fig. 8 shows the threshold displacement energies of $W_{38}Ta_{36}Cr_{15}V_{11}$ and pure W in several typical directions. The threshold displacement energy of $W_{38}Ta_{36}Cr_{15}V_{11}$ is calculated 100 times in each direction, and the data point in each direction in the figure represents the mean, while the error bar represents the standard deviation. The figure shows that the threshold displacement energy of $W_{38}Ta_{36}Cr_{15}V_{11}$ is lower than that of pure W. This means that the atoms in $W_{38}Ta_{36}Cr_{15}V_{11}$ can be displaced from their original lattice site more
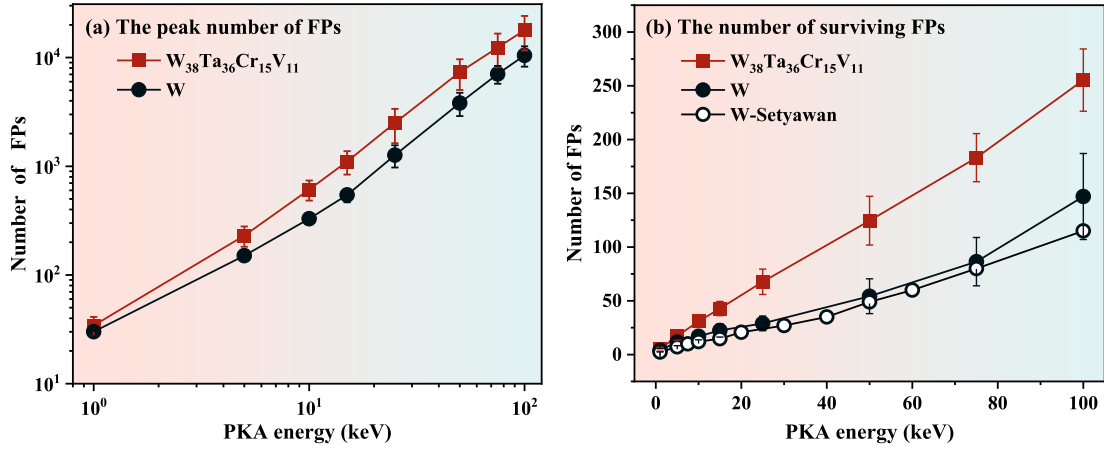
Fig. 7. (a) The average number of FPs at the thermal spike and (b) the average number of surviving FPs at the end of the cascade in $W_{38}Ta_{36}Cr_{15}V_{11}$ and W as a function of PKA energy. The data points reprent the means, and the error bars represent the standard deviations after averaging over all cascades for each case. The data in W obtained from Setyawan et al.'s study [71] is provided here for comparison.
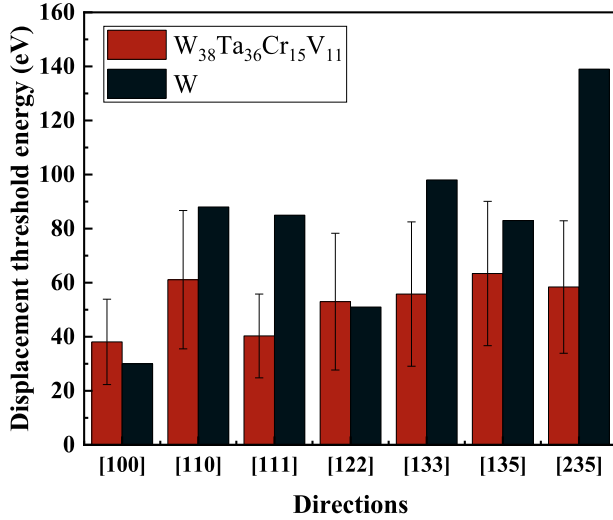

Fig. 8. Threshold displacement energy in several typical directions in $W_{38}Ta_{36}Cr_{15}V_{11}$ and W. The threshold displacement energy of $W_{38}Ta_{36}Cr_{15}V_{11}$ is calculated 100 times in each direction, and the data point in each direction in the figure represents the mean, while the error bar represents the standard deviation.

easily than the atoms in W. By using the solid-liquid coexistence method [73], the melting temperature of $W_{38}Ta_{36}Cr_{15}V_{11}$ was determined to be 3350 ± 50 K and that of W was determined to be 4350 ± 50 K. The lower melting point of $W_{38}Ta_{36}Cr_{15}V_{11}$ results in a larger melted cascade region, and thus, a higher number of FPs was detected at the thermal spike.

The number of surviving FPs at the end of the cascade in $W_{38}Ta_{36}Cr_{15}V_{11}$ was more than that in pure W. This is mainly due to the differences in the defect formation energies. The higher the values are, the more energy is required to create the same amount of defects. Fig. 9 shows the distribution of vacancy and interstitial formation energy in $W_{38}Ta_{36}Cr_{15}V_{11}$. Both vacancy formation energy and interstitial formation energy were calculated for 400 times. As shown in the figure, the blue dashed line represents the average value, while the black dashed lines in Fig. 9(a) and (b) represent the vacancy formation energy and the formation energy of the most stable self-interstitial in W, respectively. The formation energies of vacancy and interstitial in $W_{38}Ta_{36}Cr_{15}V_{11}$ exhibit wide distributions. The average vacancy formation energy is 3.0 eV, which is less than the 3.4 eV vacancy formation energy in pure W. The average interstitial formation energy is 3.7 eV, which is much lower

than the interstitial formation energies in pure W (9.5–11.2 eV).

Table. 8. shows the recombination rate of defects in $W_{38}Ta_{36}Cr_{15}V_{11}$ and W under different PKA energies that was calculated as follows:

$$\eta = \frac{N_{peak} - N_{final}}{N_{peak}} \times 100\%$$

where, N_{peak} denotes the number of FPs at the thermal spike, and N_{final} denotes the number of surviving FPs at the end of the cascade. As shown in Table 8, the recombination rates of defects are comparable in both materials. Besides, the values of η are very high at 92%–98%, except for the lowest PKA energy of 1 keV (about 85%). This is because 1 keV is too low to induce a strong heat spike, so the defect annihilation at this energy is limited compared to the other energy cases.

Fig. 10 displays the fraction of defects in clusters at the end of the cascade (last snapshot) for both vacancies and interstitials in $W_{38}Ta_{36}Cr_{15}V_{11}$ and W as a function of cascade energy. The clustered interstitial fraction in $W_{38}Ta_{36}Cr_{15}V_{11}$ is significantly lower than that in W. $W_{38}Ta_{36}Cr_{15}V_{11}$ has an interstitial cluster fraction of 10% to 30%, whereas W has an interstitial cluster fraction of 40% to 80%. The clustered vacancy fraction ranges between 25% and 45%. $W_{38}Ta_{36}Cr_{15}V_{11}$ has a slightly higher clustered vacancy fraction than W. When the PKA energy is 100 keV, the vacancy clustering fraction in the two materials is approximately 45%.

The detailed size distributions of the vacancy and interstitial clusters obtained with different PKA energies in $W_{38}Ta_{36}Cr_{15}V_{11}$ and W are presented in Figs. 11 and 12. The data were obtained by averaging over all cascades at each energy. The error bars represent the standard deviations after averaging over all cascade events for each case. Under different PKA energies, clusters with size less than 7 were found to be the most abundant. The cluster size increases as the PKA energy rises. The number and size of vacancy clusters formed in $W_{38}Ta_{36}Cr_{15}V_{11}$ are greater than those in pure W when the PKA energy is 1 keV, 5 keV, 10 keV, 15 keV, 25 keV, and 50 keV. When the PKA energy is 75 keV or 100 keV, the average number of vacancy clusters in $W_{38}Ta_{36}Cr_{15}V_{11}$ with sizes of 2–6, 7–14, 15–50, and 51–100 is more than that in pure W, whereas the average number of vacancy clusters in $W_{38}Ta_{36}Cr_{15}V_{11}$ with sizes of 101–300 is less than that in pure W. In terms of interstitial clusters, the number of large interstitial clusters (cluster size greater than 7) in $W_{38}Ta_{36}Cr_{15}V_{11}$ is lower than in pure W, and the size of the largest interstitial clusters is significantly smaller in $W_{38}Ta_{36}Cr_{15}V_{11}$. For example, when the PKA energy was 100 keV, the average number of interstitial clusters with a size of 50+ in $W_{38}Ta_{36}Cr_{15}V_{11}$ was 0.02 (1 such cluster is created in 50 cascade events), while the corresponding number in W was 0.56 (28 such clusters are created in 50 cascade
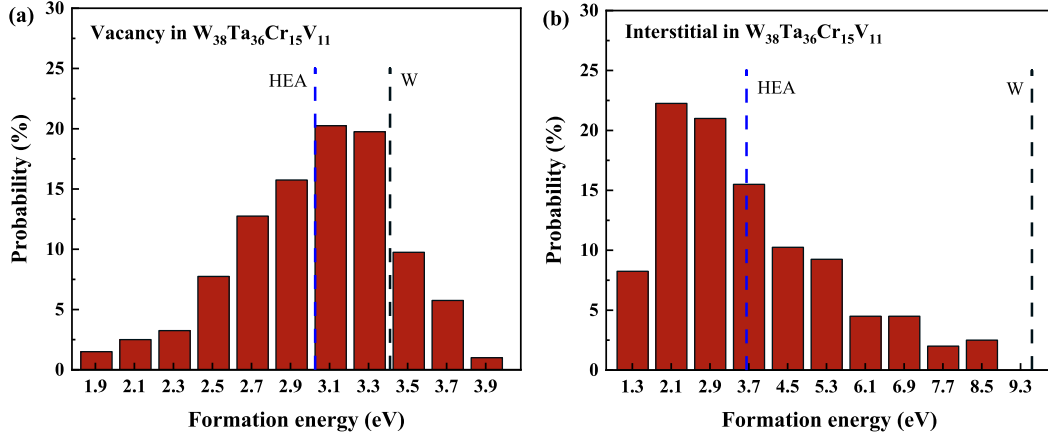
Fig. 9. Distribution of (a) vacancy formation energies and (b) interstitial formation energies in $W_{38}Ta_{36}Cr_{15}V_{11}$. The number of calculations is 400. The blue dashed line represents the average value. The black dashed lines in Fig. 9(a) and (b) represent the vacancy formation energy and the formation energy of the most stable self-interstitial in W, respectively.

Table. 8
Recombination rate of defects in $W_{38}Ta_{36}Cr_{15}V_{11}$ and W under different PKA energies. Values in brackets denote the standard deviations after averaging over all cascades for each case.

	$W_{38}Ta_{36}Cr_{15}V_{11}$	W
1 keV	85.1% (4.6%)	86.4% (5.7%)
5 keV	91.9% (2.9%)	92.1% (2.5%)
10 keV	94.5% (2.3%)	94.7% (1.4%)
15 keV	95.7% (1.8%)	95.7% (1.6%)
25 keV	96.7% (1.9%)	97.5% (1.0%)
50 keV	97.9% (1.4%)	98.4% (0.7%)
75 keV	98.2% (1.1%)	98.7% (0.5%)
100 keV	98.3% (0.8%)	98.6% (0.5%)

events). Under this PKA energy, the largest interstitial clusters contain 53 atoms for $W_{38}Ta_{36}Cr_{15}V_{11}$ and 237 atoms for pure W.

Further investigation of the dislocation loops showed that the number of dislocation loops in $W_{38}Ta_{36}Cr_{15}V_{11}$ was significantly lower than that in pure W. The dislocation loops produced in the two materials were all $1/2<111>$ interstitial dislocation loops, except for one $\langle 100 \rangle$ interstitial dislocation loop and one $\langle 100 \rangle$ vacancy dislocation loop found in pure W at 100 keV. Fig. 13 shows the size distribution of interstitial dislocation loops formed in $W_{38}Ta_{36}Cr_{15}V_{11}$ and W. Each data was calculated from the sum of 50 cascade events. The number of dislocation loops produced in pure W at PKA energies of 25 keV, 50 keV, 75 keV, and 100 keV was 3, 22, 54, and 75, respectively, while the number of

dislocation loops produced in $W_{38}Ta_{36}Cr_{15}V_{11}$ was 0, 2, 0, and 6, respectively. Collision cascades in $W_{38}Ta_{36}Cr_{15}V_{11}$ are less likely to result in the formation of dislocation loops compared to pure W.

Fig. 14 shows the fraction of different types of atoms in the surviving interstitials of $W_{38}Ta_{36}Cr_{15}V_{11}$ produced by PKA energies from 1 keV to 100 keV. The data points represent the mean values, while the error bars represent the standard deviations after averaging over all cascades for each case. As shown in the figure, the concentration of Cr and V atoms in defects after cascade is significantly higher than their corresponding concentration in the $W_{38}Ta_{36}Cr_{15}V_{11}$ system, showing an aggregation tendency. The concentrations of Cr atom and V atom in the interstitials are about 60% and 30%, respectively; these values are higher than the concentrations of 15% and 11% in the $W_{38}Ta_{36}Cr_{15}V_{11}$ system. The concentrations of W atom and Ta atom in the interstitials are both approximately 15%, which are lower than the system concentrations of 38% and 36%, respectively. This is because Cr- and V-containing interstitial dumbbells exhibit lower formation energies than W- and Ta-containing ones, as shown in Fig. 5.

4. Conclusions

In this work, a semi-empirical Finnis-Sinclair interatomic potential for W–Ta–Cr–V was developed; this is an important step toward an atomic-scale investigation of W-based HEAs. The primary radiation damage in $W_{38}Ta_{36}Cr_{15}V_{11}$ was investigated using the developed potential by running collision cascade simulations with primary knock-on
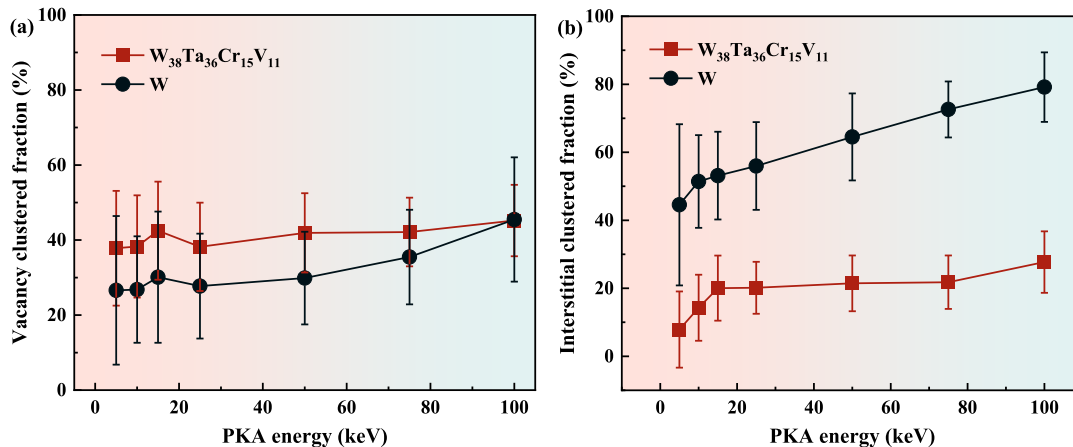

Fig. 10. Clustered fraction of vacancies (a) and interstitials (b) versus PKA energy for cascades in $W_{38}Ta_{36}Cr_{15}V_{11}$ and W.
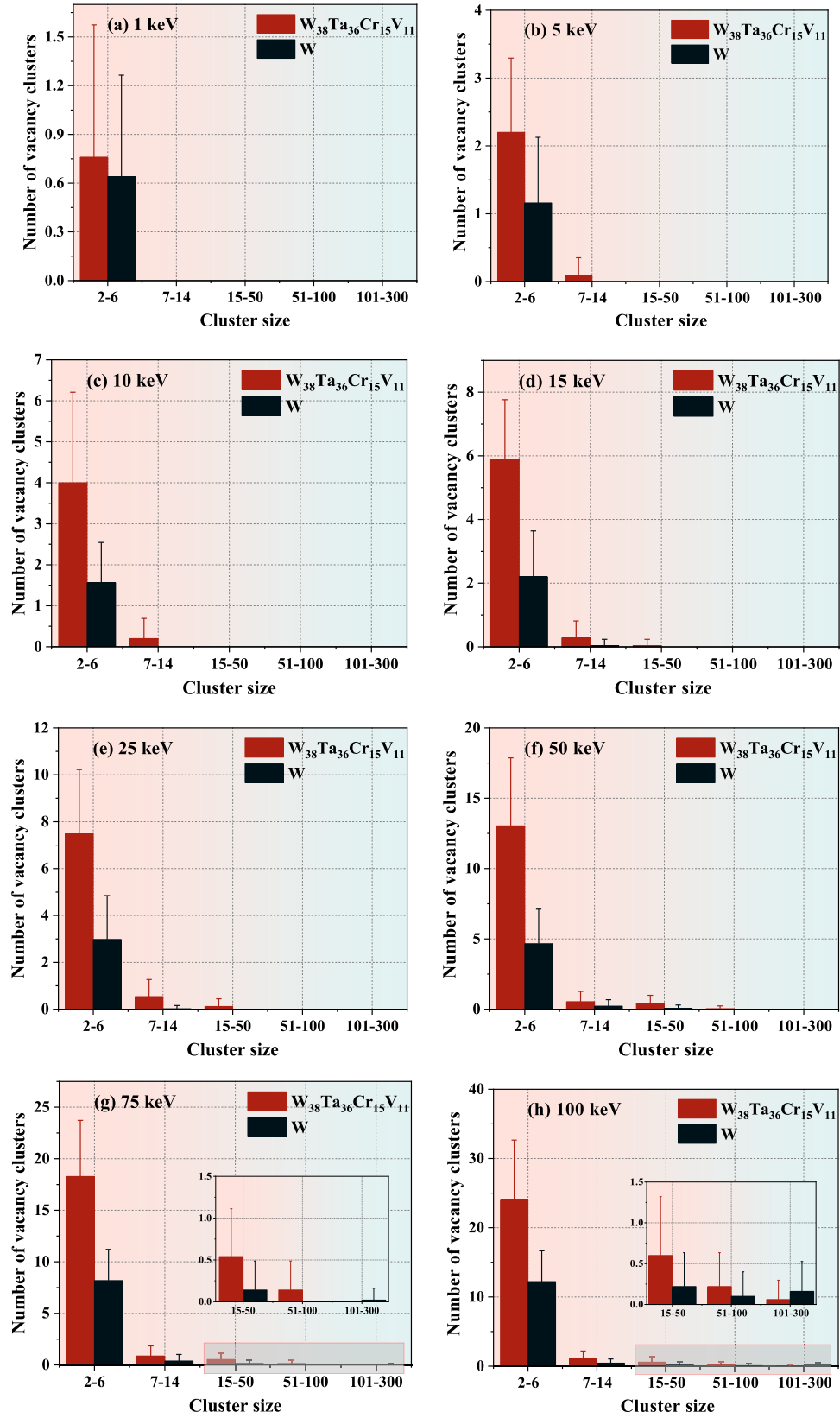
Fig. 11. Size distribution of vacancy clusters in $W_{38}Ta_{36}Cr_{15}V_{11}$ and W produced by PKA energies from 1 keV to 100 keV. The data points represent the means, and the error bars represent the standard deviations after averaging over all cascades for each case.
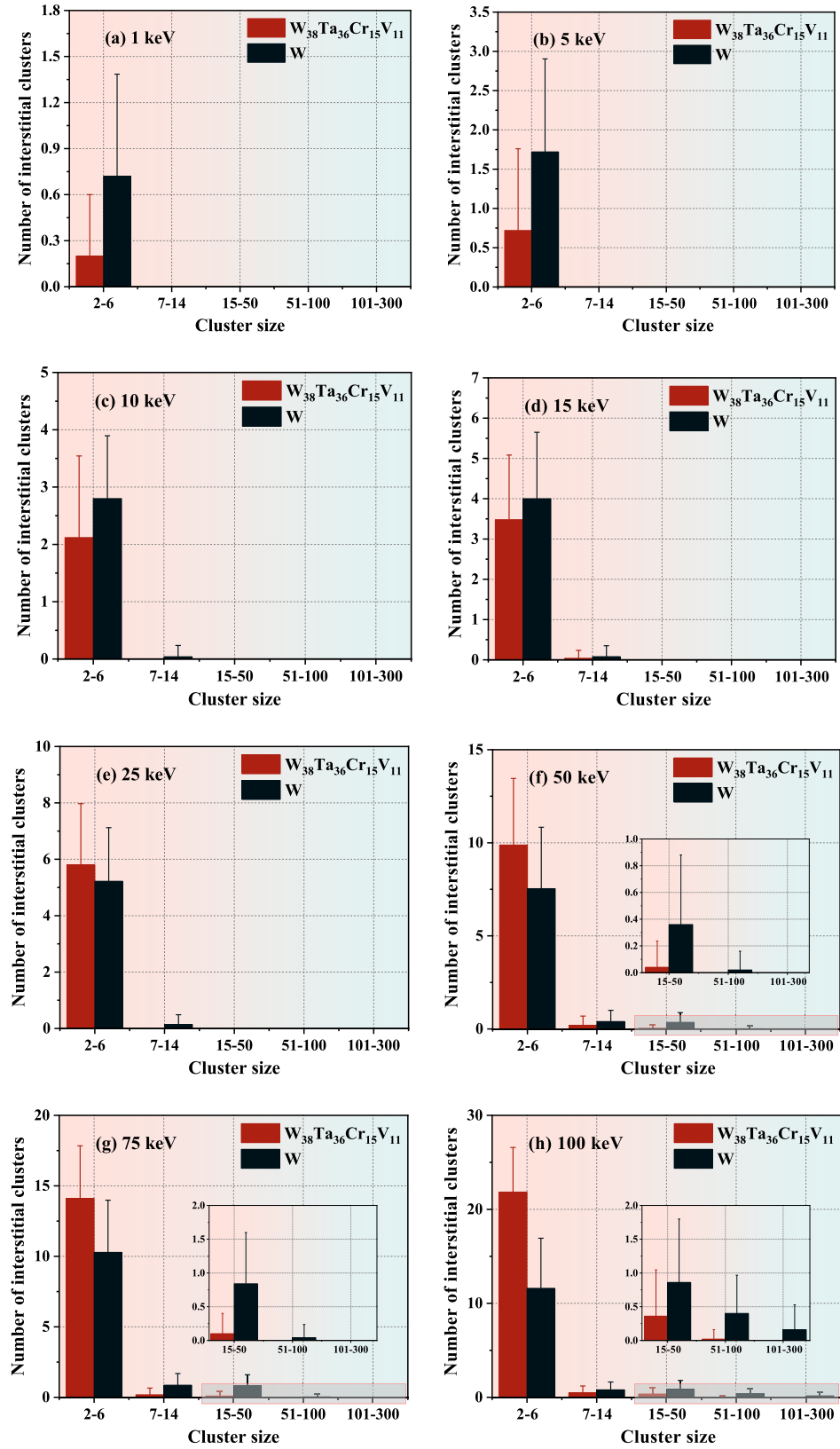
Fig. 12. Size distribution of interstitial clusters in $W_{38}Ta_{36}Cr_{15}V_{11}$ and W produced by PKA energies from 1 keV to 100 keV. The data points represent the means, and the error bars represent the standard deviations after averaging over all cascades for each case.
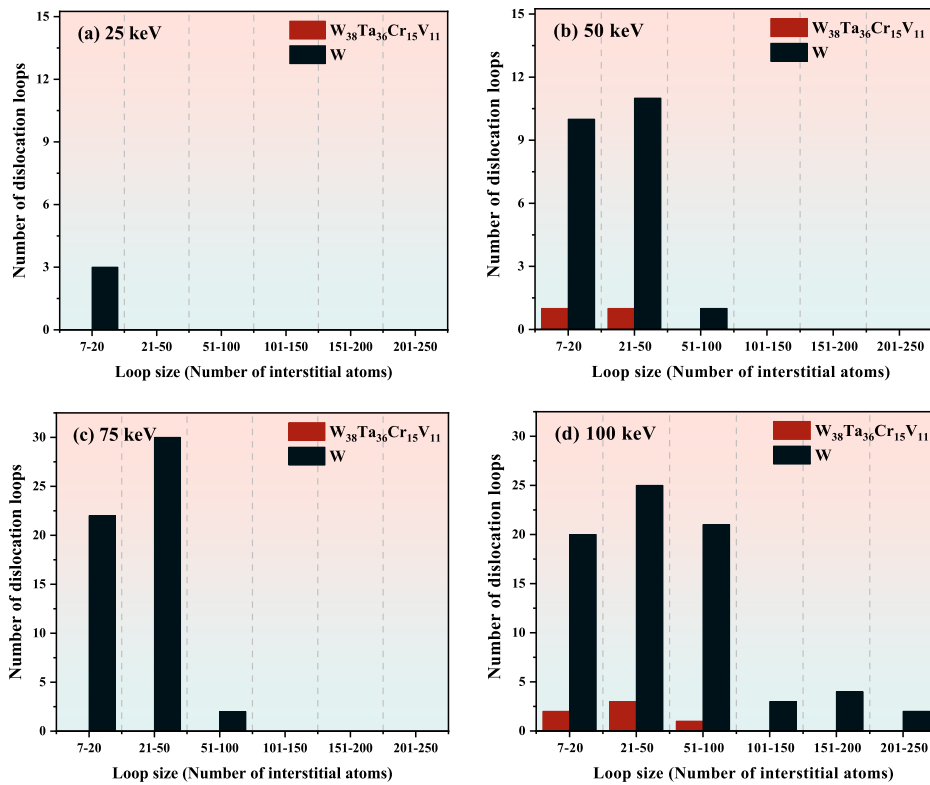
Fig. 13. Size distribution of interstitial loops formed in $W_{38}Ta_{36}Cr_{15}V_{11}$ and W after (a) 25 keV, (b) 50 keV, (c) 75 keV, and (d) 100 keV cascades. Each data is calculated from the sum of 50 cascade events.
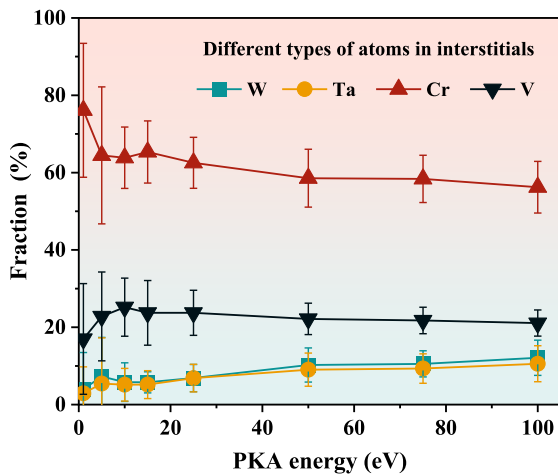

Fig. 14. Fraction of different types of atoms in all surviving interstitials of $W_{38}Ta_{36}Cr_{15}V_{11}$ produced by PKA energies from 1 keV to 100 keV. The data points represent the means, and the error bars represent the standard deviations after averaging over all cascades for each case.

atom energies ranging from 1 keV to 100 keV. Our findings showed that the number of FPs at the thermal spike and the number of surviving FPs at the end of the cascade in $W_{38}Ta_{36}Cr_{15}V_{11}$ are more than those in pure W, mainly due to the lower threshold displacement energy, melting point, and formation energy of point defects in $W_{38}Ta_{36}Cr_{15}V_{11}$. No significant difference in defect recombination rate between $W_{38}Ta_{36}Cr_{15}V_{11}$ and pure W was observed within the time scale of collision cascade simulation. The clustered vacancy fraction of $W_{38}Ta_{36}Cr_{15}V_{11}$ was slightly higher than that of W. For high PKA energies of 75 keV and 100 keV, the average number of large vacancy

clusters (cluster size greater than 100) in $W_{38}Ta_{36}Cr_{15}V_{11}$ is less than that in pure W. The clustered interstitial fraction of $W_{38}Ta_{36}Cr_{15}V_{11}$ is significantly lower than that of W. $W_{38}Ta_{36}Cr_{15}V_{11}$ has smaller interstitial clusters and fewer dislocation loops formed by collision cascade, indicating good radiation resistance at the primary damage stage. Cr- and V-containing interstitials in $W_{38}Ta_{36}Cr_{15}V_{11}$ have a lower formation energy than other interstitials. After the cascade, the concentration of Cr and V atoms in defects is significantly higher than their corresponding concentration in the system, suggesting an aggregation tendency. Overall, the simulation results were qualitatively consistent with the experimental ion irradiation results. The experiment revealed no evidence of irradiation-induced dislocation loops, but rather Cr-rich and V-rich second-phase particles. This demonstrates the reliability of the constructed interatomic potential. The W–Ta–Cr–V potential can be further developed to include He to study the helium behavior in W-based HEAs. The current collision cascade results provide insights into the primary damage of W-based HEA system under irradiation and should provide reliable guidance for describing the primary damage source terms needed in the kinetic models used to simulate radiation-induced microstructural evolution.

CRediT authorship contribution statement

Yangchun Chen: Investigation, Methodology, Formal analysis, Validation, Funding acquisition, Writing – original draft, Writing – review & editing. **Xichuan Liao:** Formal analysis, Methodology, Validation. **Rongyang Qiu:** Formal analysis, Methodology, Validation. **Lixia Liu:** Formal analysis, Methodology, Validation. **Wangyu Hu:** Conceptualization, Formal analysis, Methodology, Validation. **Huiqiu Deng:** Conceptualization, Funding acquisition, Resources, Supervision, Writing – review & editing.

Declaration of Competing Interest

The authors declare that they have no known competing financial interests or personal relationships that could have appeared to influence the work reported in this paper.

Data availability

Data will be made available on request.

Acknowledgments

References

[1] G.S. Was, D. Petti, S. Ukai, S. Zinkle, Materials for future nuclear energy systems, J. Nucl. Mater. 527 (2019), 151837.

[2] S. Wurster, N. Baluc, M. Battabyal, et al., Recent progress in R&D on tungsten alloys for divertor structural and plasma facing materials, J. Nucl. Mater. 442 (2013) S181–S189.

[3] G. Zhuang, G.Q. Li, J. Li, et al., Progress of the CFETR design, Nucl. Fusion 59 (2019), 112010.

[4] A. Hasegawa, M. Fukuda, T. Tanno, et al., Neutron irradiation behavior of tungsten, Mater. Trans. 54 (2013) 466–471.

[5] M. Rieth, S.L. Dudarev, S.M. Gonzalez de Vicente, et al., Recent progress in research on tungsten materials for nuclear fusion applications in Europe, J. Nucl. Mater. 432 (2013) 482–500.

[6] S. Kajita, W. Sakaguchi, N. Ohno, et al., Formation process of tungsten nanostructure by the exposure to helium plasma under fusion relevant plasma conditions, Nucl. Fusion 49 (2009) 95005.

[7] L. Romaner, C. Ambrosch-Draxl, R. Pippan, Effect of rhenium on the dislocation core structure in tungsten, Phys. Rev. Lett. 104 (2010), 195503.

[8] M. Battabyal, R. Schäublin, P. Spätig, et al., W-2wt.%Y_2O_3 composite: microstructure and mechanical properties, Mater. Sci. Eng. A 538 (2012) 53–57.

[9] H. Kurishita, S. Kobayashi, K. Nakai, et al., Development of ultra-fine grained W–(0.25–0.8)wt%TiC and its superior resistance to neutron and 3 MeV He-ion irradiations, J. Nucl. Mater. 377 (2008) 34–40.

[10] O. El-atwani, S. Gonderman, S. Suslov, et al., Early stage damage of ultrafine-grained tungsten materials exposed to low energy helium ion irradiation, Fusion Eng. Des. 93 (2015) 9–14.

[11] A. Xu, C. Beck, D.E. Armstrong, et al., Ion-irradiation-induced clustering in W–*Re* and W–*Re*–Os alloys: a comparative study using atom probe tomography and nanoindentation measurements, Acta Mater. 87 (2015) 121–127.

[12] O. El-Atwani, K. Hattar, J.A. Hinks, et al., Helium bubble formation in ultrafine and nanocrystalline tungsten under different extreme conditions, J. Nucl. Mater. 458 (2015) 216–223.

[13] J. Reiser, M. Rieth, A. Möslang, et al., Tungsten (W) laminate pipes for innovative high temperature energy conversion systems, Adv. Eng. Mater. 17 (2015) 491–501.

[14] J. Hohe, P. Gumbsch, On the potential of tungsten-vanadium composites for high temperature application with wide-range thermal operation window, J. Nucl. Mater. 400 (2010) 218–231.

[15] L.H. Zhang, Y. Jiang, Q.F. Fang, et al., Toughness and microstructure of tungsten fibre net-reinforced tungsten composite produced by spark plasma sintering, Mater. Sci. Eng. A 659 (2016) 29–36.

[16] O. El-Atwani, N. Li, M. Li, et al., Outstanding radiation resistance of tungsten-based high-entropy alloys, Sci. Adv. 5 (2019) eaav2002.

[17] X. Wang, H. Huang, J. Shi, et al., Recent progress of tungsten-based high-entropy alloys in nuclear fusion, Tungsten 3 (2021) 143–160.

[18] T.X. Li, J.W. Miao, E.Y. Guo, et al., Tungsten-containing high-entropy alloys: a focused review of manufacturing routes, phase selection, mechanical properties, and irradiation resistance properties, Tungsten 3 (2021) 181–196.

[19] S. Chen, C. Qi, J. Liu, et al., Recent advances in W-containing refractory high-entropy alloys—an overview,, Entropy 24 (2022) 1553.

[20] O.A. Waseem, J. Lee, H.M. Lee, et al., The effect of Ti on the sintering and mechanical properties of refractory high-entropy alloy Ti_xWTaVCr fabricated via spark plasma sintering for fusion plasma-facing materials, Mater. Chem. Phys. 210 (2018) 87–94.

[21] O.A. Waseem, H.J. Ryu, Helium ions irradiation analysis of $W_{0.5}(TaTiVCr)_{0.5}$ for application as a future fusion plasma-facing material, Mater. Chem. Phys. 260 (2021), 124198.

[22] O.N. Senkov, G.B. Wilks, J.M. Scott, et al., Mechanical properties of $Nb_{25}Mo_{25}Ta_{25}W_{25}$ and $V_{20}Nb_{20}Mo_{20}Ta_{20}W_{20}$ refractory high entropy alloys, Intermetallics 19 (2011) 698–706.

[23] O.A. Waseem, H.J. Ryu, Powder metallurgy processing of a W_xTaTiVCr high-entropy alloy and its derivative alloys for fusion material applications, Sci. Rep. 7 (2017) 1–14.

[24] O.A. Waseem, K.B. Woller, F.B. Sweidan, et al., Effects of F^{3+} ion implantation on the properties of W and $W_{0.5}(TaTiVCr)_{0.5}$ for depth marker-based plasma erosion analysis, Nucl. Mater. Energy 25 (2020), 100806.

[25] S. Alvi, O.A. Waseem, F. Akhtar, High temperature performance of spark plasma sintered $W_{0.5}(TaTiVCr)_{0.5}$ Alloy, Metals 10 (2020) 1512 (Basel).

[26] O.A. Waseem, H.J. Ryu, W0.5TaTiVCr-based composite reinforced with W-mesh for fusion plasma-facing applications, Funct. Compos. Struct. 2 (2020), 015004.

[27] O. El-Atwani, A. Alvarado, K. Unal, et al., Helium implantation damage resistance in nanocrystalline W-Ta-V-Cr high entropy alloys, Mater. Today Energy 19 (2021), 100599.

[28] O. El Atwani, H.T. Vo, M.A. Tunes, et al., A quinary WTaCrVHf nanocrystalline refractory high-entropy alloy withholding extreme irradiation environments, Nat. Commun. 14 (2023) 2516.

[29] K. Nordlund, S.J. Zinkle, A.E. Sand, et al., Primary radiation damage: a review of current understanding and models, J. Nucl. Mater. 512 (2018) 450–479.

[30] X.G. Li, C. Chen, H. Zheng, et al., Complex strengthening mechanisms in the NbMoTaW multi-principal element alloy, npj, Comput. Mater. 6 (2020) 70.

[31] J. Byggmästar, K. Nordlund, F. Djurabekova, Modeling refractory high-entropy alloys with efficient machine-learned interatomic potentials: defects and segregation, Phys. Rev. B 104 (2021), 104101.

[32] M.W. Finnis, J.E. Sinclair, A simple empirical N-body potential for transition metals, Philos. Mag. A 50 (1984) 45–55.

[33] G.J. Ackland, R. Thetford, An improved N-body semi-empirical model for body-centred cubic transition metals, Philos. Mag. A 56 (1987) 15–30.

[34] Y. Chen, Y.H. Li, N. Gao, et al., New interatomic potentials of W, *Re* and W-*Re* alloy for radiation defects, J. Nucl. Mater. 502 (2018) 141–153.

[35] Y. Chen, J. Fang, L. Liu, et al., The interactions between rhenium and interstitial-type defects in bulk tungsten: a combined study by molecular dynamics and molecular statics simulations, J. Nucl. Mater. 522 (2019) 200–211.

[36] Y. Chen, J. Fang, L. Liu, et al., Development of the interatomic potentials for W–Ta system, Comput. Mater. Sci. 163 (2019) 91–99.

[37] Y. Chen, X. Liao, N. Gao, et al., Interatomic potentials of W–V and W–Mo binary systems for point defects studies, J. Nucl. Mater. 531 (2020), 152020.

[38] R. Qiu, Y. Chen, X. Liao, et al., Finnis–sinclair-type potential for atomistic simulation of defects behaviour in V–Ti–Ta ternary system, J. Nucl. Mater. 557 (2021), 153231.

[39] R.A. Johnson, D.J. Oh, Analytic embedded atom method model for bcc metals, J. Mater. Res. 4 (1989) 1195–1201.

[40] G. Bonny, R.C. Pasianot, Gauge transformations to combine multi-component many-body interatomic potentials, Philos. Mag. Lett. 90 (2010) 559–563.

[41] X. Liao, H. Gong, Y. Chen, et al., Interatomic potentials and defect properties of Fe-Cr-Al alloys, J. Nucl. Mater. 541 (2020), 152421.

[42] R. Qiu, Y. Chen, X. Liao, et al., Development of a semi-empirical interatomic potential appropriate for the radiation defects in V-Ti-Ta-Nb high-entropy alloy, J. Phys. Condens. Matter 35 (2023), 055701.

[43] J.F. Ziegler, J.P. Biersack, U. Littmark, The Stopping and Range of Ions in Matter, Pergamon, New York, 1985.

[44] S. Kirkpatrick, C.D. Gelatt, M.P. Vecchi, Optimization by simulated annealing, Science 220 (1983) 671–680.

[45] J.H. Rose, J.R. Smith, F. Guinea, et al., Universal features of the equation of state of metals, Phys. Rev. B 29 (1984) 2963.

[46] S. Plimpton, Fast parallel algorithms for short-range molecular dynamics, J. Comput. Phys. 117 (1995) 1–19.

[47] A. Stukowski, Visualization and analysis of atomistic simulation data with OVITO-the open visualization tool, Model. Simul. Mater. Sci. Eng. 18 (2010), 015012.

[48] K. Nordlund, R.S. Averback, Point defect movement and annealing in collision cascades, Phys. Rev. B 56 (1997) 2421–2431.

[49] A. Fellman, A.E. Sand, J. Byggmästar, et al., Radiation damage in tungsten from cascade overlap with voids and vacancy clusters, J. Phys. Condens. Matter 31 (2019), 405402.

[50] J. Byggmästar, F. Granberg, K. Nordlund, Effects of the short-range repulsive potential on cascade damage in iron, J. Nucl. Mater. 508 (2018) 530–539.

[51] A. Stukowski, V.V. Bulatov, A. Arsenlis, Automated identification and indexing of dislocations in crystal interfaces, Model. Simul. Mater. Sci. Eng. 20 (2012), 085007.

[52] C. Kittel, Introduction to Solid State Physics, Wiley, New York, 2005 eighth ed.

[53] G. Simmons, H. Wang, Single Crystal Elastic Constants and Calculated Aggregate properties: A Handbook, The MIT Press, Cambridge, MA, 1971 second ed.

[54] A. Dewaele, P. Loubeyre, M. Mezouar, Refinement of the equation of state of tantalum, Phys. Rev. B 69 (2004), 092106.

[55] F.H. Featherston, J.R. Neighbours, Elastic constants of tantalum, tungsten, and molybdenum, Phys. Rev. 130 (1963) 1324–1333.

[56] D. Nguyen-Manh, A.P. Horsfield, S.L. Dudarev, Self-interstitial atom defects in bcc transition metals: group-specific trends, Phys. Rev. B 73 (2006), 020101.

[57] Y. Mishin, A.Y. Lozovoi, Angular-dependent interatomic potential for tantalum, Acta Mater. 54 (2006) 5013–5026.

[58] X. Yi, M.L. Jenkins, M.A. Kirk, et al., In-situ TEM studies of 150keV W+ ion irradiated W and W-alloys: damage production and microstructural evolution, Acta Mater. 112 (2016) 105–120.

[59] F. Ferroni, X. Yi, K. Arakawa, et al., High temperature annealing of ion irradiated tungsten, Acta Mater. 90 (2015) 380–393.

[60] R. Alexander, M.C. Marinica, L. Proville, et al., Ab initio scaling laws for the formation energy of nanosized interstitial defect clusters in iron, tungsten, and vanadium, Phys. Rev. B 94 (2016), 024103.

[61] X.B. Wu, X.S. Kong, Y.W. You, et al., Effects of alloying and transmutation impurities on stability and mobility of helium in tungsten under a fusion environment, Nucl. Fusion 53 (2013), 073049.

[62] W.L. Yan, H.B. Zhou, S. Jin, et al., Dissolution energetics and its strain dependence of transition metal alloying elements in tungsten, J. Nucl. Mater. 456 (2015) 260–265.

[63] W. Setyawan, G. Nandipati, R.J. Kurtz, Ab initio study of interstitial cluster interaction with *Re*, Os, and Ta in W, J. Nucl. Mater. 484 (2017) 30–41.

[64] L. Gharaee, P. Erhart, A first-principles investigation of interstitial defects in dilute tungsten alloys, J. Nucl. Mater. 467 (2015) 448–456.

[65] Y.W. You, X.S. Kong, X.B. Wu, et al., Clustering of transmutation elements tantalum, rhenium and osmium in tungsten in a fusion environment, Nucl. Fusion 57 (2017), 086006.

[66] X.S. Kong, X.B. Wu, Y.W. You, et al., First-principles calculations of transition metal–solute interactions with point defects in tungsten, Acta Mater. 66 (2014) 172–183.

[67] C.S. Becquart, C. Domain, Solute-point defect interactions in bcc systems: focus on first principles modelling in W and RPV steels, Curr. Opin. Solid State Mater. Sci. 16 (2012) 115–125.

[68] T. Suzudo, T. Tsuru, A. Hasegawa, First-principles study of solvent-solute mixed dumbbells in body-centered-cubic tungsten crystals, J. Nucl. Mater. 505 (2018) 15–21.

[69] D. Sobieraj, J.S. Wróbel, T. Rygier, et al., Chemical short-range order in derivative Cr–Ta–Ti–V–W high entropy alloys from the first-principles thermodynamic study, Phys. Chem. Chem. Phys. 22 (2020) 23929.

[70] S. Zhao, Defect properties in a VTaCrW equiatomic high entropy alloy (HEA) with the body centered cubic (bcc) structure, J. Mater. Sci. Technol. 44 (2020) 133–139.

[71] W. Setyawan, G. Nandipati, K.J. Roche, et al., Displacement cascades and defects annealing in tungsten, Part I: defect database from molecular dynamics simulations, J. Nucl. Mater. 462 (2015) 329–337.

[72] N. Juslin, B.D. Wirth, Interatomic potentials for simulation of He bubble formation in W, J. Nucl. Mater. 432 (2013) 61–66.

[73] J.R. Morris, C.Z. Wang, K.M. Ho, et al., Melting line of aluminum from simulations of coexisting phases, Phys. Rev. B 49 (1994) 3109.